Azimuthal Instabilities of an Annular Combustor with Different Swirling Injectors

Preethi Rajendram Soundararajan, D. Durox, Antoine Renaud, Sébastien Candel

GTP-22-1357

Azimuthal instabilities of an annular combustor with different swirling injectors

Preethi Rajendram Soundararajan [1]*, Daniel Durox [1], Antoine Renaud [1], Sébastien Candel [1]

[1]Laboratoire EM2C, CNRS, CentraleSupélec, Université Paris-Saclay, 3, rue Joliot Curie, 91192 Gif-sur-Yvette cedex, France

Email: preethi.rajendram-soundararajan@centralesupelec.fr

ABSTRACT

Experiments are carried out on the laboratory-scale MICCA-Spray annular combustor to examine the effects of swirlers on combustion instabilities. This system comprises sixteen spray-swirl injectors and gives rise to instabilities coupled by azimuthal modes. Five types of swirlers producing clockwise rotation and varying in swirl numbers and pressure drops are considered. These swirlers can be broadly categorized into two groups, lower-swirl, and higher-swirl groups, based on their swirl numbers. An arrangement where clockwise and counterclockwise swirlers alternate is also studied. Experiments are performed systematically with liquid heptane at five levels of thermal power and six equivalence ratios. Results reveal that none of the swirlers in the lower-swirl category exhibit instability in the operating region considered, whereas the higher-swirl units feature strong azimuthal instabilities that trace an overall limit cycle envelope with a few short and random bursts. Among the higher-swirl group, a higher pressure drop swirler is associated with a broader instability map. This shows that the transition to instability mainly depends on the swirl number through its effect on the flame structure and that the pressure drop adds to further variations in amplitude and frequency of oscillation. The spin ratio time series indicate that the modes are of mixed type and that their distribution depends on the operating condition. On specifically comparing the spin ratio distribution between a full set of clockwise rotating swirlers (CR) and a configuration where clockwise and counterclockwise rotating swirlers (CCR) are alternatively placed, it is found that there is no definite statistical preference for spin ratio linked to the effect of bulk swirl. In some cases, however, the CCR configuration promotes a broader distribution of spin ratios centered around the standing mode ($s = 0$) while the CR setup favors azimuthal modes spinning in the counterclockwise direction. An attempt is made to interpret the occurrence of instabilities by making use of flame describing functions (FDFs) measured in a single-injector combustor. It is found that the FDFs corresponding to

*Address all correspondence to this author.

the two swirler categories (lower-swirl and higher-swirl) are relatively distinct. The observed behavior is tentatively interpreted using an instability analysis in which the injector and upstream plenum are represented by an impedance that shifts the band of instability. The unstable behavior is then linked to the relative position of the FDF phase with respect to the instability band in the frequency range corresponding to the expected azimuthal mode frequency. The phase and gain of the FDF notably depend on the swirl number, and it is possible to distinguish, for the present configuration, a category of low swirl number injectors inducing stable operation and another category of high swirl number units leading to oscillations.

Keywords: Annular combustor, Azimuthal instabilities, Spray flame, Swirl injector, Flame describing function.

1 INTRODUCTION

Combustion instabilities have been the subject of an intense research effort [1, 2], with much of the more recent work focused on gas turbine applications. In these systems, the combustor geometry is mostly annular, and the coupling modes are predominantly azimuthal [3]. It is generally considered that these modes are the most dangerous because they are less well-damped and also because they correspond to the lowest eigenfrequencies where flames are most sensitive to disturbances. These azimuthal modes, in turn, induce axial velocity fluctuations in each injector [4], a process that dominantly leads to heat release rate fluctuations. Experiments carried out on lab-scale and industrial annular combustors [5–8], numerical simulations [4, 9–12], and theoretical analysis [13, 14] have provided a wealth of information on azimuthal coupling. Other investigations aim to develop active and passive control techniques [15–18] to reduce such instabilities. This article is specifically concerned with effects related to the swirling injector. The injector unit [19, 20] is known to determine the flame structure and dynamical characteristics, and it is important to document its influence on azimuthal combustion instabilities. This could help unravel the mechanisms of instabilities associated with swirling injectors and might, in turn, help identify injector architectures that are less sensitive to disturbances and less prone to instabilities.

Before moving further, it is worth considering some of the past research efforts carried out on annular combustors and the influence of swirler on acoustic instabilities to give a context for the present work and identify the existing knowledge gap. A large eddy simulation (LES) of a full aeronautical combustor was carried out in [10] to capture the azimuthal modes of this combustor. Results revealed that the amplitude of azimuthal modes varies with time, resulting in pressure fluctuations changing between purely standing and spinning modes. It was also found that the presence of a bulk swirling convection velocity resulted in slow rotation of the standing mode. The effect of injector spacing on instabilities was analyzed in [5, 21] on an annular combustor with flames stabilized by a bluff-body. The time evolution of the pressure variations indicated repeated switching between standing and spinning modes similar to [10]. It was found that for larger separation distances between injectors, each flame unit behaved independently and adopted a helical structure of heat release rate. The effect of bulk swirl motion on instabilities was investigated in [5]. The configuration with alternating swirl directions resulted in statistically preferred standing modes, while for the arrangement where all swirlers rotated in the same direction, the statistical preference depended on the operating conditions considered and the direction of spin dominantly depended on the bulk swirl direction. Early studies were carried out with matrix burners in the lab-scale annular combustor MICCA. Several

pure azimuthal modes, such as standing, spinning [22], and slanted [23] modes, were observed in this system. Experiments were also carried out on this combustor to identify the effect of symmetry breaking by partially blocking the injectors or changing their geometry [8].

At this point, it is also useful to identify the role of the injection units in the mechanism leading to combustion instabilities. Several studies indicate the presence of a strong interaction between the flow behavior in a swirl combustor and combustion instability (for example, [24]). This reveals a possibility of developing control techniques by altering the flow structures [25] through modification of the swirler geometry. Few researchers have pursued this, but such studies are limited only to simplified single burner test rigs. For example, the effect of inlet swirl number was studied in [26] using LES, and it was observed that strong swirling flows resulted in transverse acoustic oscillations, whereas with weak swirl, longitudinal instabilities prevailed. Komarek et al. [27] attempted to identify the effect of swirl number fluctuations by varying the axial position of the swirl generator. Through the combination of experiments and numerical simulations, it was observed that the position of the swirl generator has a strong impact on the flame's dynamical response. Another study that considered the effect of swirl number was reported in [28]. Experiments with two different swirl numbers indicated that the normalized pressure and heat release rate oscillations were more intense in the stronger swirl number case than in the weaker swirl configuration. Recently, Zhang et al. [29] performed LES on a premixed swirl-stabilized combustor and found changes in the regions of instability depending on the swirl number value. It was noted that the corner recirculation zones played a major role in inducing heat release rate fluctuations compared to the central recirculation zone. Apart from the dependence on swirl number, the work carried out in [30] revealed the effect of swirler pressure drop on combustion instabilities. A recent study by the same authors [31] in a single-injector combustor shows that the longitudinal self-sustained instabilities strongly depended on the swirler type used. A low-order model based on injector impedance using flame describing function (FDFs) was also shown to predict these instabilities. FDFs from single-injector systems have also been used to successfully predict the instabilities of annular combustors equipped with matrix burners featuring laminar flames [12]. But the predictions are less precise in [7] as the specific dynamics of spray-swirl injectors were not considered.

The above review shows that the swirler effect on instabilities has been investigated in single-injector combustors, but to our knowledge, such studies have not been carried out in annular combustors. The current investigation would thus help in bridging several knowledge gaps. (1) What happens when the swirl number and pressure drop of the injector unit are systematically varied in an annular combustor? Such knowledge would help develop swirlers that are less susceptible to instabilities. (2) What happens to the modal structure in a configuration where co- and counter-rotating swirlers are alternating compared to a configuration where all the swirlers are co-rotating? (3) Can a simplified single-injector setup capture some of the features exhibited by the multi-flame annular combustor where there are flame-flame interactions?

Experiments reported in this article address the above questions by systematically documenting instabilities observed in the lab-scale MICCA-Spray annular combustor. The experimental setup is presented in Section 2. The stability map of the annular combustor with the various swirler configurations is presented in Section 3, followed by a discussion of the modal structure between a fully co-rotating configuration and an alternate co- and counter-rotating configuration in Section 4. Results from a complementary single-injector setup, SICCA-Spray, with the various swirlers are finally presented

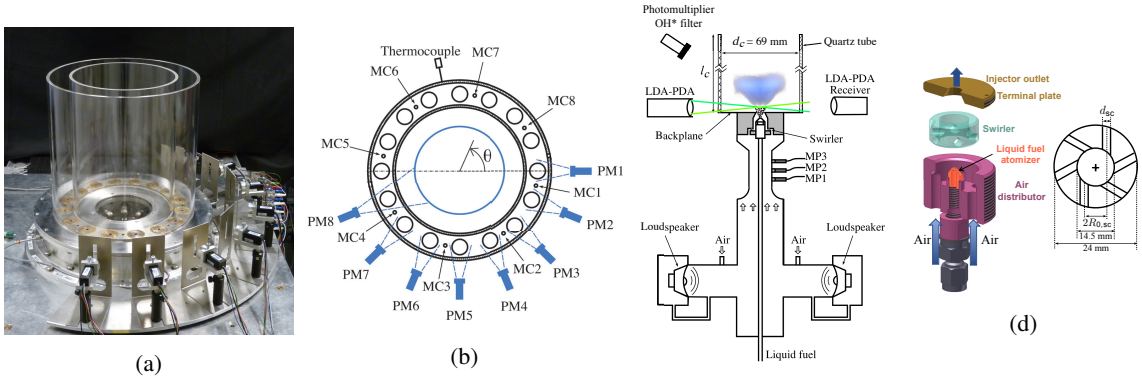

Fig. 1: (a) Photograph of the MICCA-Spray setup. The height of the combustion chamber is maintained at 400 mm for both the inner and the outer chamber walls. (b) Schematic top view of the combustion chamber showing the locations of chamber microphones (MCx) and photomultipliers (PMx). The azimuthal angle θ is positive along the counterclockwise direction and its baseline is taken along the centerline of injector 1. Adapted from [7, 32]. (c) Schematic diagram of complementary single-injector setup SICCA-Spray. (d) An exploded view of the injector unit with its various components together with a schematic drawing of the swirler.

in Section 5, along with a discussion on how they can help analyze the instabilities observed in the annular system.

2 EXPERIMENTAL SETUP OF MICCA-SPRAY

The experimental setup of the lab-scale annular combustor MICCA-Spray is shown in Fig. 1 (a) & (b). Only the main features of the test rig are described here, and the readers are referred to [7] for a more detailed description. The test rig consists of an annular plenum connected to the annular combustion chamber through sixteen swirling injectors. The injectors consist of an air distributor which supplies air from the plenum to the swirler followed by a terminal plate having a conical section with 8 mm outlet diameter. These injectors feature a high value of swirl number and abrupt area changes resulting in strong pressure drops across the swirler, thus making them only weakly transparent to acoustic waves. An exploded view of the injector with its various components and a schematic drawing of the swirler is shown in Fig. 1 (d). In the present study, liquid heptane is used as fuel and is delivered into the chamber through a simplex atomizer mounted on the injector. The atomizer disperses finely atomized fuel droplets into the chamber as a hollow cone spray in the presence of air flow. The MICCA-Spray chamber consists of two concentric, cylindrical quartz tubes of height 400 mm. The inner wall has an outer diameter of 300 mm, and the outer wall has an inner diameter of 400 mm, resulting in a mean diameter of 350 mm. Air flow rate is controlled through a Bronkhorst EL-FLOW mass flow meter, which has a relative accuracy of 0.6%, and the fuel flow rate is controlled by a Bronkhorst CORI-FLOW controller, which has a relative accuracy of 0.2%. Eight Brüel & Kjær microphones are mounted on the chamber (marked as MCx in Fig. 1 (b)). These microphones are placed on waveguides whose ports are flush-mounted on the chamber backplane to prevent direct contact of the microphones with the hot chamber environment. The waveguide ports are located between every two injectors, and they are terminated by a 25 m long tube to prevent any wave reflections. The microphone signals are acquired at a sampling frequency of $f_s = 32\,768$ Hz for a total time period of $T_0 = 16$ s. Additionally, the chamber is equipped with eight photomultipliers that capture the light intensity fluctuations, but the result of these measurements is not discussed in what follows.

Table 1: Swirler characteristics measured under cold flow in the single-injector combustor SICCA-Spray (refer to Section 5) at an air flow rate of $\dot{m}_{\text{air}} = 2.6\,\text{g s}^{-1}$ and 2.5 mm above chamber backplane. S_N represents the experimentally obtained swirl number and Δp represents the pressure drop of the injector. σ is the head loss coefficient defined by $\Delta p = \frac{1}{2}\sigma\rho_0 u_b^2$, where u_b is the bulk velocity at the injector exit and ρ_0 is the density. d_{sc} is the diameter of the swirler channels and $R_{0,sc}$ is the distance between the axis of a channel and the axis of the swirler.

Category	Swirler (-)	S_N (-)	Δp (kPa)	σ (-)	d_{sc} (mm)	$R_{0,sc}$ (mm)
Lower-swirl	707	0.60	3.65	3.33	4.0	4.6
	712	0.59	4.50	4.10	3.0	2.3
Higher-swirl	716/816	0.70	5.74	5.23	3.5	4.7
	726	0.74	6.00	5.47	3.5	5.5
	727	0.74	5.70	5.20	3.5	5.1

For the present study, five different radial swirlers featuring six tangential channels are tested. The swirlers are named 707, 712, 716, 726, and 727, and their characteristics are provided in Tab. 1. The swirlers' geometrical parameters are given in terms of d_{sc}, which is the diameter of the swirler channels, and $R_{0,sc}$, which is the radial distance between the axis of a channel and the axis of the swirler. These two geometrical parameters are suitably varied to obtain different swirl numbers S_N and pressure drops Δp or head loss coefficient σ. The swirlers can be grouped into two categories based on their swirl number: the lower-swirl category comprising swirlers 707 and 712, and the higher-swirl category comprising the rest of the swirlers. Each group also contains swirlers with the same swirl number values but different pressure drops. The swirlers 707 and 712 have nearly the same swirl number, but the pressure drops are not identical. Their swirl number is lower than the swirler numbers of the higher-swirl category. Among the higher-swirl category, the swirlers 726 and 727 have the same swirl numbers but a slightly different pressure drop, while the swirlers 716 and 727 have almost the same pressure drop, but 727 has a slightly higher swirl number. In addition to the five swirling injectors, a combination of clockwise rotating (716-type) and counterclockwise rotating (namely, 816) swirlers are placed alternatively to understand the effect of overall bulk swirl on instabilities. Swirler 816 is completely identical to swirler 716 except in the swirl direction.

3 STABILITY MAP OF MICCA-SPRAY ANNULAR COMBUSTOR

The stability map of the MICCA-Spray annular combustor is obtained by considering five levels of thermal power $\mathcal{P}$ and, at each level, six different equivalence ratios ϕ are tested, resulting in a total of thirty operating points per swirler. At each operating point, the fuel flow rate is fixed, and the air flow rate is systematically varied to obtain different equivalence ratios. The stability map of MICCA-Spray is represented in terms of two parameters, amplitude and frequency of instability, to suitably represent the first azimuthal-first longitudinal 1A1L azimuthal modes exhibited in the assessed operating points. Considering a $e^{-i\omega t}$ time harmonic convention for the acoustic waves, at any instant t, the acoustic pressure measured by the chamber microphones can be represented as:

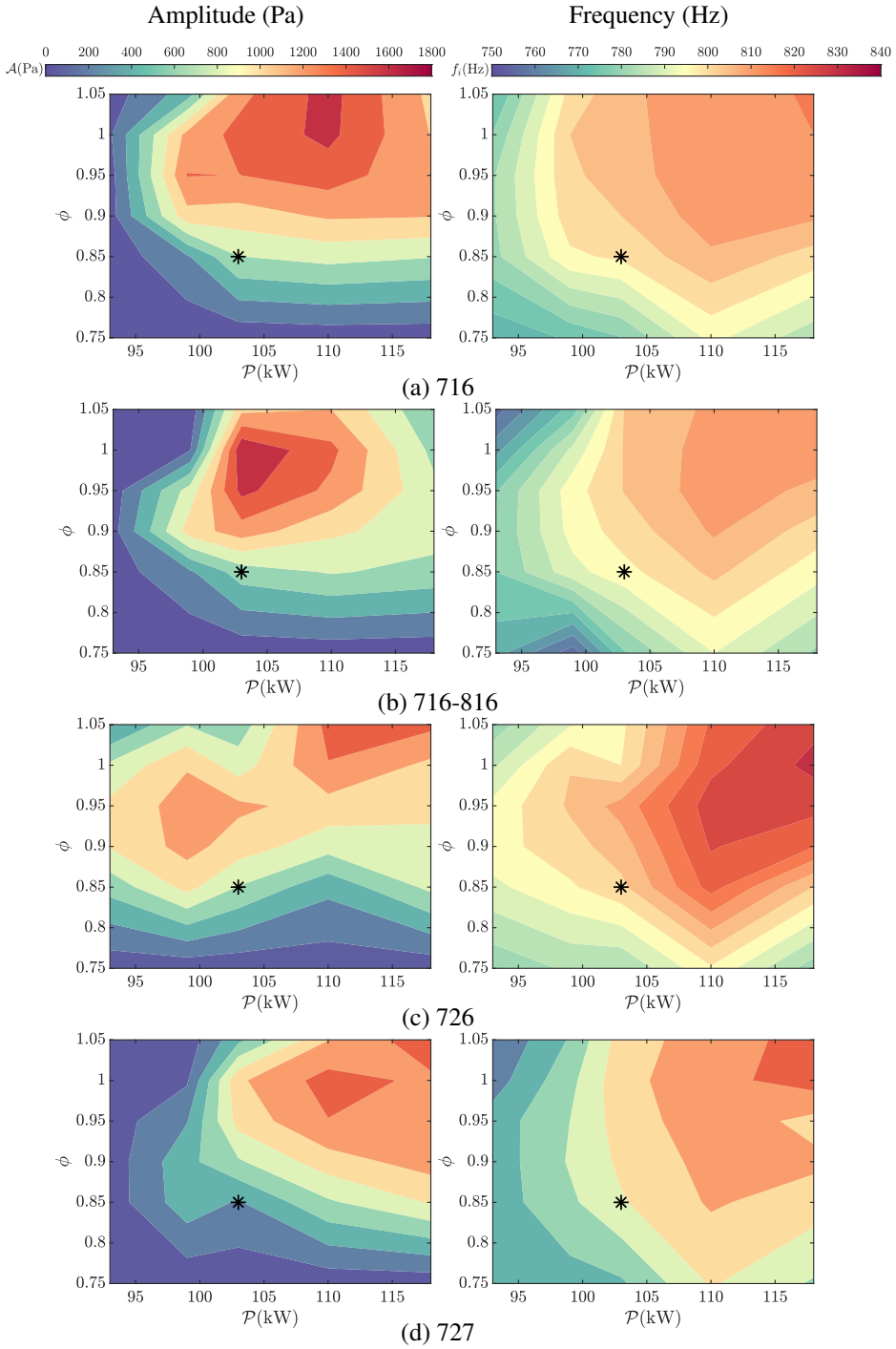

Fig. 2: Amplitude (left) and frequency (right) stability map of MICCA-Spray for the different swirlers in higher-swirl category. The swirlers in the lower-swirl category (707 and 712) are always stable in the assessed operating zone and hence are not shown here. The black star on the stability map refers to the operating conditions of the complementary single-injector combustor described in Section 5.

$$p_c'(\theta,t) = A^+ \exp(i\theta - i\omega t) + A^- \exp(-i\theta - i\omega t) \tag{1}$$

In this expression, p'_c represents the instantaneous pressure measured by the microphones, A^+ and A^- designate counterclockwise and clockwise spinning waves respectively of the 1A1L mode, $\omega = 2\pi f_i$ is the angular frequency, and θ is the azimuthal angle which is considered positive in the counterclockwise direction. The instantaneous signals recorded by the eight chamber microphones can be used to determine the wave amplitudes A^+ and A^- and deduce an indicator of instability that is spatially averaged over the annulus and temporally averaged over the duration of acquisition [7]. This amplitude $\mathcal{A} = (|A^+|^2 + |A^-|^2)^{1/2}$ is proportional to the root mean square (RMS) amplitude and is independent of the structure of the unstable mode. $\mathcal{A}$ is used to compare the instability between the different swirlers along with the instability frequency f_i, which is the peak frequency from the power spectrum of the microphone signals. The power spectral densities are obtained using Welch's periodogram method by considering 64 windows with 50% overlap between windows, resulting in a frequency resolution of $\Delta f \approx 2\,\text{Hz}$. The microphone signals are bandpass-filtered between 500 Hz and 1100 Hz, and the time-resolved analytical signals are obtained through the Hilbert transform. The wave amplitudes are then reconstructed up to the third order in azimuthal harmonics [32]. In addition to comparing the amplitude and frequency of instability, the spin ratio s_r is calculated to identify the structure of the azimuthal instabilities and is given by,

$$s_r = \frac{|A^+| - |A^-|}{|A^+| + |A^-|} \tag{2}$$

A value $s_r = 1$ corresponds to a counterclockwise spinning wave, $s_r = -1$ represents a clockwise spinning wave, and $s_r = 0$ pertains to a standing azimuthal wave.

The behavior of the swirlers in the lower-swirl category (707 and 712) is special as they do not exhibit any azimuthal instability in the domain of interest ($\mathcal{P}$ between 93-118 kW and ϕ between 0.75-1.05), and the fluctuating pressure amplitude remains below 50 Pa. On the contrary, all the swirlers in the higher-swirl category exhibit unstable behavior. Although the various swirlers have similar geometries, a minor change resulting in the reduction of swirl number improves the stability of the annular combustor. This study indicates that there is a critical value $0.6 < S_{N\text{crit}} < 0.7$ such that injectors with low swirl $S_N < S_{N\text{crit}}$ yield stable operation, while units with swirl numbers exceeding this critical value $S_{N\text{crit}} < S_N$ lead to oscillations in certain ranges of operating parameters. It is worth noting, however, that this categorization is specific to the present configuration and may not be generally applicable. For the different swirlers in the higher swirl category, stability maps representing the amplitude and frequency of instability are displayed in Fig. 2. The data obtained at the thirty operating points are interpolated to derive the stability maps plotted in this figure.

A previous study by the same authors [7] reported the results of swirler 716 to identify the effect of fuel type on combustion instabilities. These results are duplicated in this article to facilitate comparison with other swirlers. The measurements were also repeated, and it was found that the stability contour shapes and their location were reproducible but with some differences in the amplitude levels caused by variations in the nature of the modes sustaining the instability. Overall, the swirlers exhibit gradual changes from stable to unstable states as the operating points are varied. On comparing the three swirlers in the higher-swirl category (716, 726, 727), minor variations in amplitude can be observed; the highest amplitude of instability

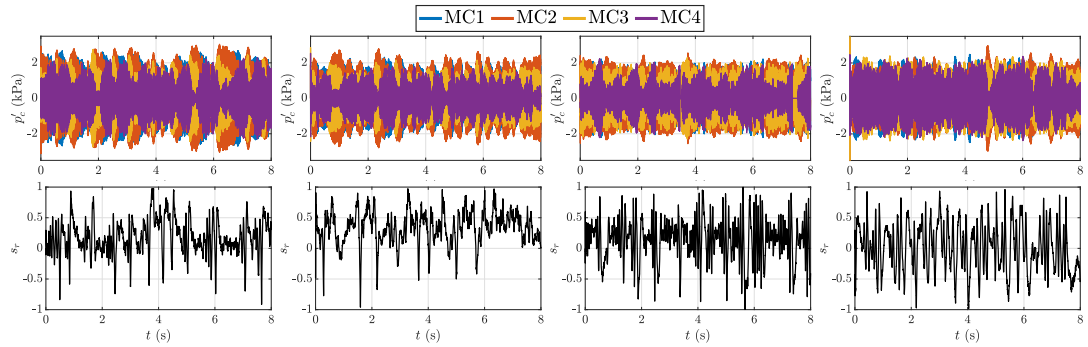

(a) 716 ($\mathcal{A} = 1653\,\text{Pa}$) (b) 716-816 ($\mathcal{A} = 1453\,\text{Pa}$) (c) 726 ($\mathcal{A} = 1392\,\text{Pa}$) (d) 727 ($\mathcal{A} = 1480\,\text{Pa}$)

$\mathcal{P} = 110\,\text{kW}$ & $\phi = 1.0$

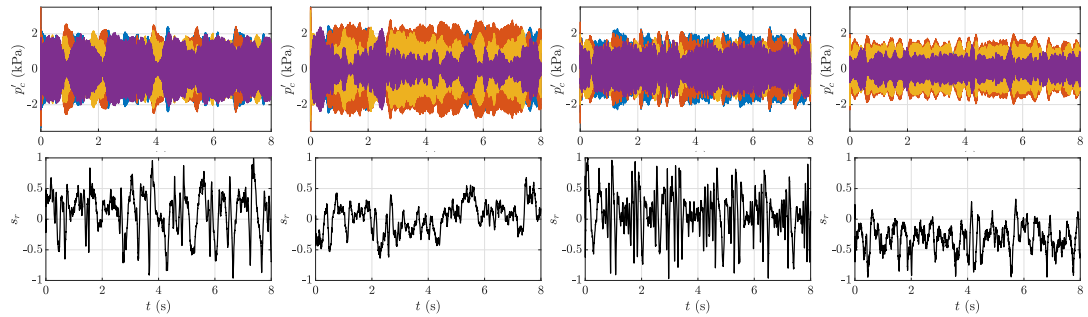

(e) 716 ($\mathcal{A} = 1397\,\text{Pa}$) (f) 716-816 ($\mathcal{A} = 1657\,\text{Pa}$) (g) 726 ($\mathcal{A} = 1241\,\text{Pa}$) (h) 727 ($\mathcal{A} = 1073\,\text{Pa}$)

$\mathcal{P} = 103\,\text{kW}$ & $\phi = 0.95$

Fig. 3: Time evolution of chamber pressure p_c' (MC1 to MC4) and spin ratio s_r for the swirlers 716, the alternate arrangement of 716-816, 726, and 727. Two operating points are chosen from the instability map where strong instability is exhibited by the four swirler configurations. The pressure-spin ratio set at the top corresponds to $\{\mathcal{P} = 110\,\text{kW}\ \&\ \phi = 1.0\}$, and the bottom set corresponds to $\{\mathcal{P} = 103\,\text{kW}\ \&\ \phi = 0.95\}$.

is exhibited by swirler 716 ($\mathcal{A}_{\text{max}} \approx 1673\,\text{Pa}$) at $\mathcal{P} = 110\,\text{kW}$ and at slightly fuel-rich conditions ($\phi = 1.05$). This is followed by swirler 727, which exhibits a maximum amplitude of $\mathcal{A}_{\text{max}} \approx 1540\,\text{Pa}$ at $\mathcal{P} = 118\,\text{kW}$, also under slightly rich conditions, and then swirler 726, which reaches the maximum amplitude of $\mathcal{A}_{\text{max}} \approx 1460\,\text{Pa}$ at both $\mathcal{P} = 118$ and $110\,\text{kW}$ for slightly rich conditions. The amplitude stability map of 727 evolves like that of 716 (Fig. 2 (a) & (d) left), while it differs from the map of 726, which has the broadest instability region among the three swirlers, exhibiting instability even at the lowest power. The swirlers 727 and 716 possess the same pressure drop, which is slightly lower than the pressure drop of 726. This observation points to the dependence of instability amplitude on the pressure drop; a higher pressure drop for the same swirl number appears to widen the region of instability. The amplitude map of 726 contains two discrete high-instability zones (red zones in Fig. 2 (c) left), one occurring at higher power and slightly richer conditions and the other occurring at lower power and leaner equivalence ratio. Swirlers 716 and 727, however, exhibit continuous high-instability regions at higher equivalence ratios and are always stable at the lowest power. All the swirlers are stable at the lowest equivalence ratio of 0.75, irrespective of the thermal power.

On comparing the frequency maps, swirlers 716 and 727 feature similar values. But with 726, the frequencies are 15 Hz higher than those of the other two swirlers. The operating point where the instability frequency is highest occurs at $\mathcal{P} = 118\,\text{kW}$ and close to stoichiometry, a set of conditions yielding the highest adiabatic flame temperature and correspondingly

the highest frequency of oscillation.

It is also interesting to examine oscillations at some points in the unstable range to compare features exhibited by the different swirlers. A first point is characterized by $\{\mathcal{P} = 110\,\text{kW}\ \&\ \phi = 1.0\}$ while the second corresponds to $\{\mathcal{P} = 103\,\text{kW}\ \&\ \phi = 0.95\}$. The pressure-time traces recorded by four chamber microphones are shown in the top rows of Fig. 3, whereas the spin ratio evolutions are plotted in the bottom rows of this figure. The pressure signals feature an overall limit cycle envelope with small, random bursts. The spin ratio randomly switches between standing and spinning modes. Such a modal behavior was previously observed in large eddy simulations [10] and in annular combustor experiments [5, 33]. At the two operating points, swirler 716 is characterized by similar spin ratio fluctuations between standing $s_r = 0$ and the two spinning modes $s_r = -1$ and +1. The spin ratio traces corresponding to 726 are also quite similar with rapid fluctuations between the different modes but centered around the standing mode $s_r = 0$, while these traces are notably different for swirler 727. At $\{\mathcal{P} = 110\,\text{kW}\ \&\ \phi = 1.0\}$, s_r rapidly oscillates between the standing and spinning modes, whereas, at $\{\mathcal{P} = 103\,\text{kW}\ \&\ \phi = 0.95\}$, it mostly oscillates between standing and clockwise spinning mode and spends almost no time in the $s_r > 0$ (counterclockwise) region.

4 INSTABILITY BEHAVIOR WITH CO- AND COUNTER-ROTATING SWIRLERS

It is now worth comparing the combustion dynamics in a configuration where all the swirlers impart clockwise rotation (all are of 716-type, referred to as CR: clockwise rotating), and a configuration where clockwise and counterclockwise rotating swirlers are alternatively placed (716-816, designated as CCR: clockwise-counterclockwise rotating). Our goal is to check whether the bulk swirl induced in the annular chamber when all swirlers rotate in the same direction influences the modal dynamics. A study of this type was already carried out by Worth & Dawson [5] in an annular system using a different class of injectors comprising a central bluff-body stabilizer and featuring a lower swirl number. As indicated in [5], the bulk rotation in the CR arrangement can be expected to be in the clockwise direction along the outer wall of the annulus and in the anticlockwise direction along the inner wall. The CR arrangement would also form a shear velocity layer between two adjacent injectors due to the opposite direction of the swirling velocity. The bulk motion would be canceled out in the CCR configuration, where co- and counter-rotating swirlers are alternatively placed.

The stability maps in Fig. 2 (a) & (b) right show that the instability frequency is the same for the two cases. This is expected since changing the swirl direction does not change the overall temperature distribution in the chamber, which, in turn, is reflected in the instability frequency. On the other hand, some changes appear in the location of the unstable domain (Fig. 2 (a) & (b) left), which is shifted towards lower thermal powers and equivalence ratios for the CCR arrangement compared to the CR arrangement. This can be better appreciated by probing the point where the maximum amplitude of oscillation occurs in these two cases. In the CR arrangement, one finds $\mathcal{A}_{\text{max}} = 1673\,\text{Pa}$ at $\mathcal{P} = 110\,\text{kW}$ and $\phi = 1.05$, while in the CCR configuration $\mathcal{A}_{\text{max}} = 1775\,\text{Pa}$ occurs at a lower thermal power of $\mathcal{P} = 103\,\text{kW}$ and a lower equivalence ratio of $\phi = 1.0$. The pressure signals plotted in Fig. 3 (a-b) & (e-f), corresponding to CR and CCR arrangements, are fairly similar with intermittent bursts along with rapid changes in the modal composition as indicated by the spin ratio evolution (in the same figures).

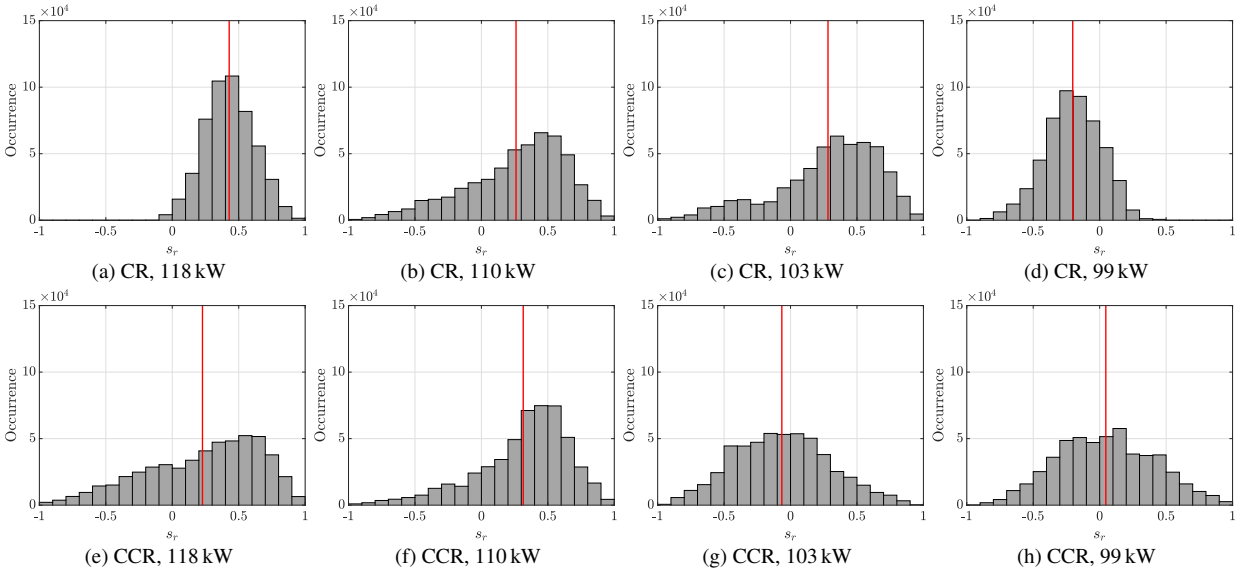

(a) CR, 118 kW (b) CR, 110 kW (c) CR, 103 kW (d) CR, 99 kW

(e) CCR, 118 kW (f) CCR, 110 kW (g) CCR, 103 kW (h) CCR, 99 kW

Fig. 4: Histogram of spin ratio occurrence comparing a configuration where all the swirlers impact clockwise rotation (CR) and a configuration where clockwise and counterclockwise rotating (CCR) swirlers are alternatively placed. The red vertical line corresponds to the mean spin ratio $\overline{s_r}$. The results are presented at four thermal powers and $\phi = 0.9$.

Previous studies on annular combustors [5, 10] indicate that when all the swirlers impart rotation in the same direction (i.e., CR configuration), the bulk swirl imposes a slow rotational motion of the nodal line of the $s_r = 0$ standing mode. Worth and Dawson [5] indicate that in the alternate anticlockwise and clockwise swirler arrangement (i.e., CCR configuration), a statistical preference towards a standing mode appears compared to the case where all swirlers induce a rotation in the same direction (i.e., all are co-rotating as in the CR configuration). To see if this is verified in the present configuration, one may examine the spin ratio statistical distributions plotted in Fig. 4 for the CR and CCR configurations corresponding to four thermal powers ($\mathcal{P}$: 118, 110, 103, 99 kW) and a single equivalence ratio $\phi = 0.9$. In these diagrams, most of the spin ratio distributions resemble a Gaussian random process with a mean and standard deviation that depend on the operating point. The preferred operating mode can be roughly deduced from the mean spin ratio $\overline{s_r}$, shown as a vertical red line. The statistical preference is mostly either a standing mode or an anticlockwise spinning mode but not a clockwise spinning mode except for the CR configuration at 99 kW, where the distribution inclines towards a clockwise spinning wave mixtures. The CCR combination has a wider distribution spanning the full range of spin ratios at most of the operating points. This might be attributed to an effect of the bulk swirl, but one observes that, at certain operating points, the CR configuration as well features a relatively broad distribution (see Fig. 4 (b) & (c)). Therefore, in contrast with [5], the present data indicate that there is no statistical preference for a particular mode. Similar data at other operating points confirm this finding, so one cannot generally infer that the presence of a bulk swirl determines the nature of the coupling mode.

5 FLAME DESCRIBING FUNCTIONS AND THEIR IMPACT

It is natural to ask whether flame describing functions (FDFs) can be used to analyze the differences in unstable behavior observed in MICCA-Spray with the various swirler units. The FDFs are determined in the single-injector combustor, namely SICCA-Spray, which represents one sector of the MICCA-Spray annular combustor. This analysis is carried out at one

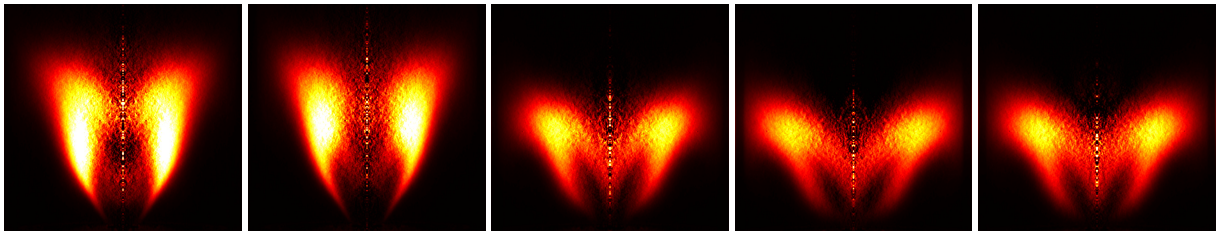

(a) 707 (b) 712 (c) 716 (d) 726 (e) 727

Fig. 5: Flame images showing OH* chemiluminescence captured in SICCA-Spray under stable conditions. An Abel inversion is applied to the averaged images captured by the camera and are displayed in false colors. $\mathcal{P}_{\text{sicca}} = 6.4\,\text{kW}$ and $\phi = 0.85$. The swirlers 707 and 712 belong to the lower-swirl category, while the other three swirlers (716, 726, 727) belong to the higher-swirl category.

operating point selected from the MICCA-Spray stability map, which is marked as a black star in Fig. 2. The annular combustor operates at a thermal power of $\mathcal{P} = 103\,\text{kW}$ and an equivalence ratio of $\phi = 0.85$. The corresponding thermal power of SICCA-Spray is $\mathcal{P}_{\text{sicca}} = 6.4\,\text{kW}$. The experimental setup shown in Fig. 1 (c) is described in some previous investigations [7, 30, 31]. The rig comprises a cylindrical quartz chamber with an inner diameter of 69 mm, allowing optical access to the flame region, and is operated with the same injectors as MICCA-Spray. Although the wall-bounded flames in SICCA-Spray do not exactly represent the flames of MICCA-Spray, where each flame is surrounded by other flames, it is concluded in a later investigation that they approximately represent the flame dynamics in MICCA-Spray to a reasonable degree [34]. This conclusion relies on a comparison between the single injector configuration and a newly developed three-injector linear test rig TICCA-Spray, where the central flame is surrounded by two side flames and more closely resembles the MICCA-Spray environment. In these three configurations, the injection to backplane surface area ratio is nearly kept constant. It is found that the FDFs measured in the single-injector rig do not coincide but are generally close to those found in the multiple injector array. Since the FDF data from the single-injector configuration (SICCA-Spray) is more thorough, it is used in what follows to interpret observations made in the annular system. Before discussing the flame response in terms of FDFs, it is logical to first examine flame shapes under steady conditions.

5.1 Flame shapes formed by the different swirlers

Flame images displayed in Fig. 5 are recorded when the SICCA-Spray combustor is in a steady state stable operation. Each image is obtained by averaging 30 frames recorded by an intensified CCD camera fitted with an OH* filter (centered at 310 nm) and applying an Abel inversion to the average image.

The overall flame shapes corresponding to the lower-swirl injectors notably differ from those formed by the higher-swirl units. The lower-swirl devices (707 and 712) establish “V” flames that are narrower and longer. Such flames would result in reduced interactions with the neighboring flames in MICCA-Spray. Between 707 and 712, the flames differ in the distribution of chemiluminescence intensity; while 707 has a relatively uniform distribution in the flame wings, 712 features a more concentrated chemiluminescence intensity close to the tip. The higher-swirl units form “M” flames that are generally wider, resulting in augmented flame-flame interactions in MICCA-Spray. The flame wing angle is lower for 716 compared to the other two swirlers (726 and 727), probably because this unit has a lower swirl number. A modest difference exists

between 726 and 727 in the two central branches, which are seen to merge at a greater distance from the outlet for 727 compared to 726. This could possibly be linked to the difference in pressure drop values, as other parameters remain the same for these two swirlers. Differences in mean flame shapes can be expected to influence the flame response to incoming disturbances, as confirmed in what follows.

5.2 Measurement of flame describing function

The flame response to external acoustic modulations is obtained in the SICCA-Spray combustor in terms of a flame describing function (FDF). In the absence of equivalence ratio fluctuations, the FDF is given by:

$$\mathcal{F} = (\dot{Q}'/\overline{\dot{Q}})/(\dot{q}_v'/\overline{\dot{q}_v}) \tag{3}$$

where $\dot{Q}'/\overline{\dot{Q}}$ designates the relative fluctuations in heat release rate, and $\dot{q}_v'/\overline{\dot{q}_v}$ represents the relative fluctuations in volume flow rate. The assumption that equivalence ratio fluctuations are negligible is verified in [31] for the injectors considered in the present study. The heat release rate fluctuations can then be measured by obtaining the intensity of chemiluminescence emitted by excited radicals such as OH* or CH*. While this is well validated for premixed flames, the case of spray flames is complicated as they may feature spatial inhomogeneities in equivalence ratio. This aspect is considered in [31], where it is concluded that these injectors behave in a quasi-premixed fashion due to the recessed position of the atomizer. Thus, for the present spray flames, chemiluminescence intensity can be used as an indicator of heat release rate. A photomultiplier fitted with an OH^* filter centered at 308 nm records the mean and fluctuating light intensities $I'(\mathrm{OH}^*)/\overline{I(\mathrm{OH}^*)}$ from the flame, which approximately represents the relative heat release rate fluctuations $\dot{Q}'/\overline{\dot{Q}}$.

The relative fluctuations in volume flow rate $\dot{q}_v'/\overline{\dot{q}_v}$ is often replaced by the relative velocity fluctuations $u'/\overline{u}$ for ease of measurement. Such a substitution is valid as long as the measurement is carried out in a region where the relative velocity fluctuations match the relative volumetric flow rate fluctuations. In several studies, velocity fluctuations are measured in the plenum. However, this lumps together the injector and flame responses and may not be appropriate when the injector is only weakly transparent to acoustic modulations [31]. It is then preferable to measure the relative velocity fluctuations at a point in the chamber where they are equivalent to relative volumetric flow rate fluctuations. This was studied in [31], and it was found that the suitable measurement position is close to the location of maximum mean axial velocity. This location is at $r = 3.5$ mm for the swirlers in the lower-swirl category (707 and 712) and at $r = 4$ mm from the center of the injector for the swirlers in the higher-swirl category (716, 726, 727) and at a height of $h = 2.5$ mm above the backplane. The axial velocity fluctuations are measured with a Dantec Dynamics 2-component phase Doppler particle analyzer (PDPA) system operating in laser Doppler anemometry mode and making use of the heptane droplets in the spray. This is adequate because the droplet size at the measurement point does not exceed a mean diameter of 8 µm, and the droplets, therefore, follow the air flow well in the frequency range of interest.

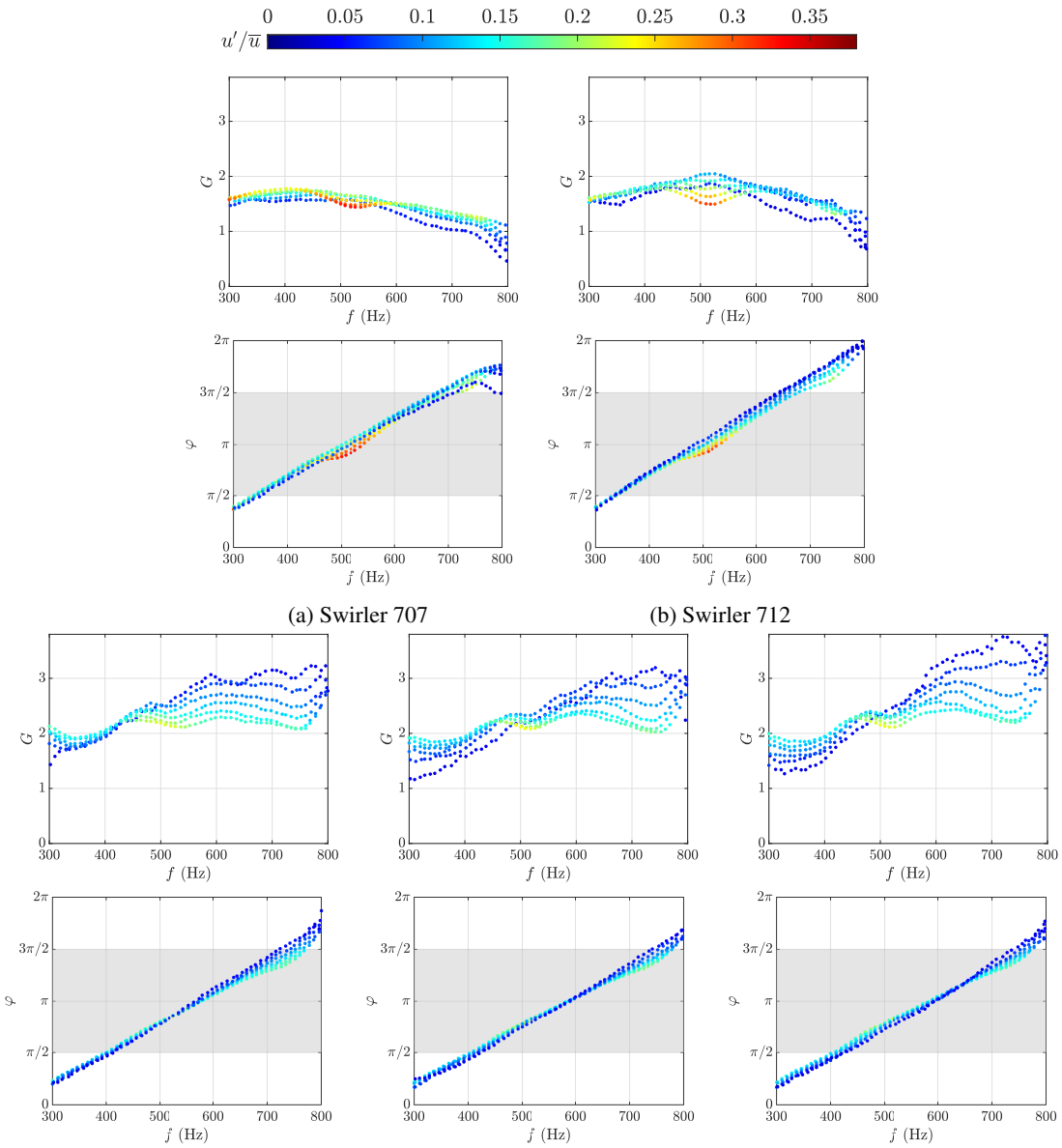

(a) Swirler 707 (b) Swirler 712

(c) Swirler 716 (d) Swirler 726 (e) Swirler 727

Fig. 6: Flame describing function represented in terms of gain G and phase φ at different levels of relative velocity fluctuation $u'/\overline{u}$ and shown for the five swirlers considered. The gray bands in the phase diagrams indicate the tentative unstable bands. It is recalled here that swirlers 707 and 712 belong to the lower-swirl category, while the other three swirlers (716, 726, 727) belong to the higher-swirl category.

The two driver units mounted at the bottom of SICCA-Spray are modulated at different frequencies and amplitudes, resulting in different levels of relative velocity fluctuations $u'/\overline{u}$ at the injector outlet to obtain the FDF gain G and phase φ. The FDFs are shown in Fig. 6 for the five swirling injectors considered in this study. The FDFs for the lower-swirl category (Fig. 6 (a) & (b)) notably differ in both gain and phase from the FDFs of the higher-swirl category (Fig. 6 (c), (d), & (e)). However, the FDFs are quite similar when the swirlers belong to the same category. On comparing the swirlers 707 and 712 (Fig. 6 (a) & (b) top), it can be observed that the overall trend in gain is preserved with some minor differences. While the gain of 707 evolves almost linearly with the velocity fluctuation levels, 712 exhibits mild variations with respect to the velocity fluctuation level close to 500 Hz in the tested amplitude range. The gain for swirler 707 features a plateau

until 600 Hz, beyond which there is a steady drop. For swirler 712, the gain mildly increases in the low frequency range (< 600 Hz) and falls beyond that frequency. Similarly, the gains of the swirlers 716, 726, and 727 exhibit the same overall behavior, rising until around 550 Hz and then reaching a plateau, especially at the higher velocity fluctuation levels. In the low frequency range, the 716 gain is nearly independent of the velocity fluctuation level but then exhibits substantial sensitivity to the excitation level beyond 500 Hz. The other two swirlers (726 and 727) feature a weak nonlinearity, first at the lower velocity fluctuation amplitudes and below 500 Hz, but this becomes more pronounced beyond this limit, similar to the 716 case. For the same level of amplifier input voltages delivered to the driver units of SICCA-Spray, 707 reaches the highest level of velocity fluctuations, with $u'/\bar{u} \approx 37\%$ at a frequency of around 500 Hz. This level is slightly lower for 712 at 31%, whereas the swirlers in the higher-swirl category feature a maximum level of about 23%. These limitations in relative modulation levels may be linked to the pressure drop. The swirlers in the higher-swirl category also feature the highest pressure drop values offering higher resistance to the incoming acoustic disturbances.

The phase of the FDF is almost linear for all of the swirlers in the amplitude range tested. A mild nonlinearity is observed around 500 Hz for 707, beyond 500 Hz for 712, and beyond 700 Hz for the higher-swirl units. The phase of the FDF essentially depends on the swirler category. In general, the higher-swirl units have similar phase functions, whereas the lower-swirl devices differ in their phase characteristics beyond 630 Hz.

5.3 Instability analysis using FDFs

The FDF framework allows for a reasonable prediction of instabilities observed in MICCA-Spray as demonstrated in [12]. For injectors that are weakly transparent to acoustic waves, like the ones considered here, it was shown more recently [31] that a low-order model may be used to predict instabilities of SICCA-Spray. The model consists of imposing an impedance ζ at the injector outlet, the phase of which determines the "unstable bands", and an experimentally determined FDF $\mathcal{F}$ to represent the flame dynamics. One may infer, from this model, a qualitative interpretation of observations made in the annular system.

The model yields unstable bands, which can be plotted in the FDF phase diagram. If the phase of the FDF at a particular frequency falls within this band, then one can predict a "potential instability" at this frequency. The location of this unstable band is predominantly decided by the phase of the impedance φ_ζ at the injector outlet, which, in turn, could be linked to the injector pressure drop, as seen in [31]. In addition, one also obtains a growth rate for the instability, which directly depends on the FDF gain. If this growth rate is greater than the damping imposed by the system, then it can be concluded that a particular operating point will be "definitely unstable" in MICCA-Spray. Using this simplified injector representation and FDF, an attempt is made to understand the instabilities of the MICCA-Spray combustor. It has been shown in [31] that for an acoustically weakly transparent injector, the impedance measured at the injector outlet takes a phase φ_ζ in the range $[3\pi/4, \pi]$ for frequencies lying between 300 and 600 Hz. This result is also obtained in [35] using a similar injector placed in a linear multi-injector test rig and submitted to transverse acoustic perturbations around 750 Hz. In the absence of information on the definite injector impedance in the annular configuration, one may tentatively assume that $\varphi_\zeta = \pi$. The corresponding unstable band lies in the range between $[\pi/2, 3\pi/2]$, and this band can be placed in the phase diagrams shown in Fig. 6 & 7 (marked

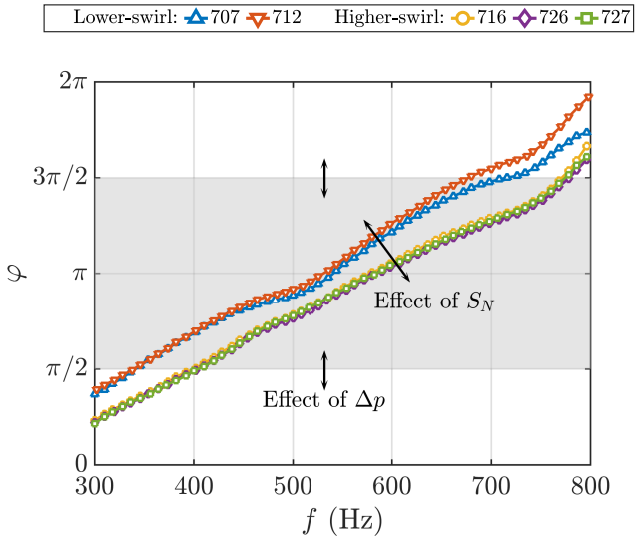

Fig. 7: FDF phase φ for the different swirlers considered in this study. Only the phase evolution of Fig. 6 corresponding to the maximum attainable relative velocity fluctuations are shown. The swirlers 707 and 712 belong to the lower-swirl category while the swirlers 716, 726, and 727 belong to the higher-swirl category.

as a gray region). As seen from the flame images in Fig. 5, the flames are longer for the lower-swirl group, whereas they are shorter and broader for the higher-swirl group. From these images, the axial location of the heat release rate barycenter a_b can be calculated and is found to be approximately at a height of 36 mm for the lower-swirl category and 30 mm for the higher-swirl category. Given that the higher-swirl group has a slightly higher maximum mean axial velocity between the different swirlers [31] (69 $\mathrm{m\,s^{-1}}$ for 716 and 58 $\mathrm{m\,s^{-1}}$ for 707 measured 2.5 mm above chamber backplane), and assuming that disturbances travel at half the maximum mean velocity [36], one can expect the lower-swirl group to have a higher time delay. This is then reflected as a comparatively higher FDF phase for the lower-swirl category, which is seen in Fig. 7, where two distinct groups of FDF phase functions can be distinguished depending on the swirler category. This figure shows the FDF phase for all the swirlers to facilitate comparison. Only the phase curves of Fig. 6 corresponding to the maximum of relative velocity fluctuations at all frequencies are shown in Fig. 7. Noting that the instabilities in MICCA-Spray coupled by the first azimuthal, first longitudinal (1A1L) mode have oscillation eigenfrequencies lying between 750 and 832 Hz, one can see that the phases for 707 and 712 cross the $3\pi/2$ upper limit of the unstable band at 700 Hz and 650 Hz respectively. This clearly indicates that the two lower-swirl units will not give rise to 1A1L instability in MICCA-Spray. For the three swirlers in the higher-swirl group, the phase of the instability band crosses the $3\pi/2$ limit at $\approx$ 790 Hz at the highest level of velocity fluctuations ($u'/\overline{u} \approx 15\%$ in Fig. 6 (c-e) bottom row). This crossing frequency is close to the 1A1L eigenfrequency providing a positive growth rate. This means that these swirlers might give rise to an instability and that their crossing frequency would then increase as the amplitude grows, while the phase would continue to be reduced and stay within the unstable band in Fig. 2 so that the oscillation corresponding to 726 would finally reach a limit cycle at a frequency of 832 Hz. Of course, this is only a tentative scenario since there is no information beyond 800 Hz and also because the unstable band has been placed in the range $[\pi/2, 3\pi/2]$. Thus, as a general guideline, one may say that the pressure drop defines the position of the unstable band, whereas the location of the phase with respect to the unstable band is mainly controlled by the swirl number,

consequently deciding the stability of the system.

One other condition for instability is to have a growth rate level that is sufficiently high to overcome the system damping rate. The growth rate increases with the FDF gain. From the gain plots in Fig. 6, a significant difference is observed between the two swirl categories. For the lower-swirl group, the gain decreases between 750 and 832 Hz and drops below one. Whereas, for the higher-swirl category, the gain increases in this range and is about two times higher than that of the lower-swirl category. The three swirlers in the higher-swirl category feature similar FDF gain values ($G_{\text{average}} \approx 2.8$), thus promoting the occurrence of instabilities in the annular combustor at this operating point and partially explaining why the swirlers in the higher-swirl category become unstable in MICCA-Spray, whereas units in the lower-swirl category are always stable.

It is also possible to infer why swirlers 716 and 727 have similar stability maps, as indicated in Section 3. These two swirlers have the same pressure drops, their FDF phase functions are identical, and their gains are roughly similar. The unstable bands will have the same location, and one may expect a common instability behavior. In contrast, the relatively high pressure drop induced by swirler 726 might shift the tentative unstable band towards higher phase values. Thus, for an FDF phase that is slightly above the upper limit of the unstable band corresponding to 716 and 727, the swirler 726 might still show an unstable operation (refer to Fig. 7). Thus, in the frequency range between 750 to 832 Hz, one can expect that 726 will feature a broader instability range, which is also confirmed by the results shown in Section 3 (Fig. 2 (c) left). In addition, the FDF phase corresponding to slightly higher frequencies would be inside the unstable band for 726. This potentially explains the comparatively higher instability frequencies in MICCA-Spray with this swirler (see Fig. 2 (c) right).

6 CONCLUSION

Systematic experiments carried out on a lab-scale annular combustor equipped with sixteen injectors are used to identify swirler effects on azimuthal combustion instabilities. The present investigation reports results obtained with five different swirlers that may be qualified as weakly transparent to acoustic waves. Their swirl numbers range from 0.59 to 0.74 with relatively high pressure drop coefficients. The swirlers are categorized based on the swirl number values into lower-swirl (swirlers 707 and 712) and higher-swirl (swirlers 716, 726, 727) groups with variations in pressure drops within each category. The swirlers in the lower-swirl group also have comparatively lower pressure drops. Experiments are carried out with liquid heptane at five thermal power and six global equivalence ratio levels (30 operating points) for each swirler. The data are then used to plot stability maps which indicate that the swirler type has a notable influence on the stability characteristics of the system. One observes that:

- None of the swirlers in the lower-swirl category feature instability at any of the thirty operating points tested. In contrast, all the swirlers in the higher-swirl category give rise to azimuthal instabilities.
- The transition to an unstable mode is mostly determined by the swirl number through its effect on flame structure. The pressure drop contributes to further variations in amplitude and frequency of oscillation.
- On comparing the swirlers in the higher-swirl category, a higher pressure loss value appears to be associated with

wider instability regions and higher oscillation frequencies in the tested range of operating conditions.

• The evolution of the spin ratio reveals that the modes are of mixed type and constantly switch between standing and spinning modes, an observation similar to [5, 10].

An additional case of alternatively-placed clockwise and counterclockwise rotating (CCR) swirlers is compared with the standard arrangement where all the swirlers are clockwise rotating (CR) to reveal possible effects of mean bulk swirl on instabilities. It is found that:

• Compared to the CR arrangement, the stability map for the CCR arrangement is shifted towards lower thermal powers and lower equivalence ratios.

• When the mean bulk swirl is absent, the spin ratio distribution features no statistical preference to standing or spinning mode.

• In some cases, the CCR configuration promotes a broader distribution of spin ratios centered around the standing mode ($s_r = 0$), while the CR arrangement appears to favor counterclockwise spinning modes.

Flame shapes and flame describing functions (FDFs) measured in a single-injector combustor, namely SICCA-Spray, representing one sector of MICCA-Spray, are employed to interpret the differences in behavior observed in the annular system at one operating point. Results show that:

• The flame shapes obtained under stable conditions are distinct for each swirler category. Swirlers in the lower-swirl category generally take a "V" shape, whereas the swirlers in the higher-swirl category take an "M" shape.

• The dynamical response of the flames represented in terms of an FDF also distinctly depends on the swirler category.

An attempt is made to qualitatively interpret instability observations in the annular combustor by making use of a simplified instability analysis combining the FDFs and impedance at the swirler outlet. A tentative instability band is defined [31], the position of which depends on the impedance, which, in turn, is expected to depend on the pressure drop of the injector. For the lower-swirl injector, one finds that the FDF phase lies outside the instability band in the frequency range of the 1A1L mode of MICCA-Spray. In the higher-swirl case, the phase is near the band upper boundary in the frequency range of the 1A1L mode, and the gain takes larger values that are about twice those of the lower-swirl units. These two features may then promote the growth of instability. As the gain decreases with the amplitude of velocity oscillations, this will lead to a limit cycle. As a general rule, one may say that the pressure drop decides the position of the unstable band, whereas the location of the FDF phase with respect to the unstable band is controlled by the swirl number, consequently deciding the stability of the system.

Appendix A: FDF phase evolution at a higher equivalence ratio

It is interesting to see whether the instability analysis developed in Section 5.3 can be used to explain observations made at a higher equivalence ratio of $\phi = 0.95$ but at the same thermal power of $\mathcal{P} = 103\,\mathrm{kW}$ in MICCA-Spray corresponding to a thermal power $\mathcal{P}_{\mathrm{sicca}} = 6.4\,\mathrm{kW}$ in SICCA-Spray. One may only consider two swirlers, 707 and 716, one from each category,

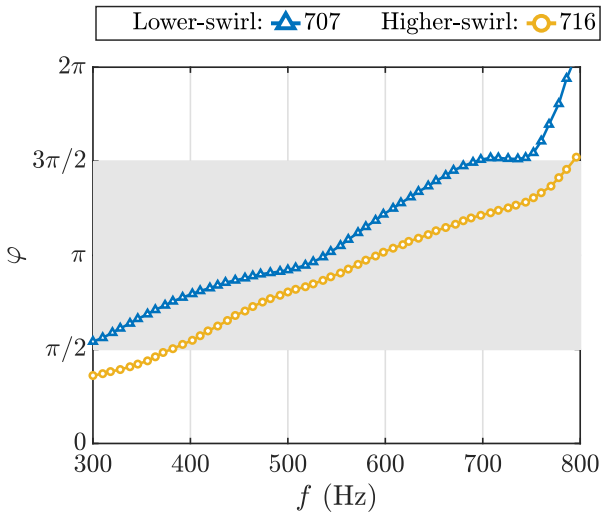

Fig. 8: FDF phase φ for swirlers 707 and 716 at $\phi = 0.95$ and $\mathcal{P}_{\text{sicca}} = 6.4\,\text{kW}$ in SICCA-Spray. Only the phase evolution with the maximum attainable relative velocity fluctuations at all frequencies are shown.

which typify the trends observed for the two swirler groups. It is also sufficient to examine the FDF phase corresponding to the highest level of relative velocity fluctuations plotted in Fig. 8 together with the tentative unstable band between $[\pi/2, 3\pi/2]$ marked in gray. The phase of 707 leaves the unstable band at 700 Hz. Since the instability frequency in MICCA-Spray corresponding to the 1A1L mode lies between 750 and 832 Hz, one can conclude that this swirler will lead to a stable operation of the annular combustor. In contrast, the phase of 716 falls within the unstable band between 380 and 800 Hz, which comprises a part of the eigenfrequencies of MICCA-Spray. When MICCA-Spray is equipped with this swirler, it may potentially become unstable. The regime will be unstable if, in addition, the gain of the FDF is sufficiently high and such that the growth rate may overcome the damping rate in the system. The present results obtained at a higher equivalence ratio substantiate the discussion in Section 5.3.

Acknowledgements

This work was supported by the European Union's Horizon 2020 research and innovation programme, Annulight with grant agreement no. 765998. The authors thank the anonymous reviewers for their many useful comments.

References

[1] Mongia, H. C., Held, T., Hsiao, G., and Pandalai, R., 2003. "Challenges and progress in controlling dynamics in gas turbine combustors". *J. Propul. Power,* **19**(5), pp. 822–829.

[2] Lieuwen, T. C., and Yang, V., 2005. "Combustion instabilities in gas turbine engines: operational experience, fundamental mechanisms, and modeling". *Am. Inst. Aeronaut. Astronaut.*

[3] Poinsot, T., 2017. "Prediction and control of combustion instabilities in real engines". *Proc. Combust. Institute,* **36**(1).

[4] Staffelbach, G., Gicquel, L., Boudier, G., and Poinsot, T., 2009. "Large eddy simulation of self excited azimuthal modes in annular combustors". *Proc. Combust. Inst.,* **32**(2), pp. 2909–2916.

[5] Worth, N. A., and Dawson, J. R., 2013. "Modal dynamics of self-excited azimuthal instabilities in an annular combustion chamber". *Combust. Flame,* **160**(11), pp. 2476–2489.

[6] Prieur, K., Durox, D., Schuller, T., and Candel, S., 2017. "A hysteresis phenomenon leading to spinning or standing azimuthal instabilities in an annular combustor". *Combust. flame,* **175**, pp. 283–291.

[7] Rajendram Soundararajan, P., Vignat, G., Durox, D., Renaud, A., and Candel, S., 2021. "Effect of different fuels on combustion instabilities in an annular combustor". *J. Eng. Gas Turb. Power,* **143**(3), p. 031007.

[8] Aguilar, J. G., Dawson, J., Schuller, T., Durox, D., Prieur, K., and Candel, S., 2021. "Locking of azimuthal modes by breaking the symmetry in annular combustors". *Combust.Flame,* **234**, p. 111639.

[9] Wolf, P., Balakrishnan, R., Staffelbach, G., Gicquel, L. Y., and Poinsot, T., 2012. "Using LES to study reacting flows and instabilities in annular combustion chambers". *Flow, Turbulence Combus.,* **88**(1), pp. 191–206.

[10] Wolf, P., Staffelbach, G., Gicquel, L. Y., Müller, J.-D., and Poinsot, T., 2012. "Acoustic and large eddy simulation studies of azimuthal modes in annular combustion chambers". *Combust. Flame,* **159**(11), pp. 3398–3413.

[11] Pankiewitz, C., and Sattelmayer, T., 2003. "Time domain simulation of combustion instabilities in annular combustors". *J. Eng. Gas Turb. Power,* **125**(3), pp. 677–685.

[12] Laera, D., Schuller, T., Prieur, K., Durox, D., Camporeale, S. M., and Candel, S., 2017. "Flame describing function analysis of spinning and standing modes in an annular combustor and comparison with experiments". *Combust. Flame,* **184**, pp. 136–152.

[13] Ghirardo, G., and Juniper, M. P., 2013. "Azimuthal instabilities in annular combustors: standing and spinning modes". *Proc. R. Soc. A: Math., Phys. Eng. Sci.,* **469**(2157), p. 20130232.

[14] Parmentier, J.-F., Salas, P., Wolf, P., Staffelbach, G., Nicoud, F., and Poinsot, T., 2012. "A simple analytical model to study and control azimuthal instabilities in annular combustion chambers". *Combust. Flame,* **159**(7), pp. 2374–2387.

[15] Steele, R. C., Cowell, L. H., Cannon, S. M., and Smith, C. E., 2000. "Passive control of combustion instability in lean premixed combustors". *J. Eng. Gas Turb. Power,* **122**(3), pp. 412–419.

[16] Krishnan, A., Sujith, R., Marwan, N., and Kurths, J., 2021. "Suppression of thermoacoustic instability by targeting the hubs of the turbulent networks in a bluff body stabilized combustor". *J. Fluid Mech.,* **916**.

[17] Noiray, N., Durox, D., Schuller, T., and Candel, S., 2009. "Dynamic phase converter for passive control of combustion instabilities". *Proc. Combust. Inst.,* **32**(2), pp. 3163–3170.

[18] Annaswamy, A. M., and Ghoniem, A. F., 2002. "Active control of combustion instability: Theory and practice". *IEEE Control Systems Magazine,* **22**(6), pp. 37–54.

[19] Huang, Y., and Yang, V., 2009. "Dynamics and stability of lean-premixed swirl-stabilized combustion". *Prog. Energy Combust. Sci.,* **35**(4), pp. 293–364.

[20] Candel, S., Durox, D., Schuller, T., Bourgouin, J.-F., and Moeck, J. P., 2014. "Dynamics of swirling flames". *Ann. Rev. Fluid Mech.,* **46**, pp. 147–173.

[21] Worth, N. A., and Dawson, J. R., 2013. "Self-excited circumferential instabilities in a model annular gas turbine combustor: Global flame dynamics". *Proc. Combust. Inst.,* **34**(2), pp. 3127–3134.

[22] Bourgouin, J.-F., Durox, D., Moeck, J. P., Schuller, T., and Candel, S., 2015. "Characterization and modeling of a spinning thermoacoustic instability in an annular combustor equipped with multiple matrix injectors". *J. Eng. Gas Turb. Power,* **137**(2), p. 021503.

[23] Bourgouin, J.-F., Durox, D., Moeck, J., Schuller, T., and Candel, S., 2015. "A new pattern of instability observed in an annular combustor: The slanted mode". *Proc. Combust. Inst.,* **35**(3), pp. 3237–3244.

[24] Steinberg, A. M., Boxx, I., Stohr, M., Meier, W., and Carter, C. D., 2012. "Effects of flow structure dynamics on thermoacoustic instabilities in swirl-stabilized combustion". *AIAA Journal,* **50**(4), pp. 952–967.

[25] Paschereit, C. O., Gutmark, E., and Weisenstein, W., 2000. "Excitation of thermoacoustic instabilities by interaction of acoustics and unstable swirling flow". *AIAA Journal,* **38**(6), pp. 1025–1034.

[26] Huang, Y., and Yang, V., 2005. "Effect of swirl on combustion dynamics in a lean-premixed swirl-stabilized combustor". *Proc. Combust. Inst.,* **30**(2), pp. 1775–1782.

[27] Komarek, T., and Polifke, W., 2010. "Impact of swirl fluctuations on the flame response of a perfectly premixed swirl burner". *J. Eng. Gas Turb. Power,* **132**(6), p. 061503.

[28] Kim, K. T., 2016. "Combustion instability feedback mechanisms in a lean-premixed swirl-stabilized combustor". *Combust. Flame,* **171**, pp. 137–151.

[29] Zhang, B., Shahsavari, M., Rao, Z., Yang, S., and Wang, B., 2021. "Thermoacoustic instability drivers and mode transitions in a lean premixed methane-air combustor at various swirl intensities". *Proc. Combust. Inst.,* **38**(4), pp. 6115–6124.

[30] Vignat, G., Durox, D., Prieur, K., and Candel, S., 2019. "An experimental study into the effect of injector pressure loss on self-sustained combustion instabilities in a swirled spray burner". *Proc. Combust. Inst.,* **37**(4), pp. 5205–5213.

[31] Rajendram Soundararajan, P., Durox, D., Renaud, A., Vignat, G., and Candel, S., 2022. "Swirler effects on combustion instabilities analyzed with measured FDFs, injector impedances, and damping rates". *Combust. Flame,* **238**(4), p. 111947.

[32] Vignat, G., Durox, D., Renaud, A., and Candel, S., 2020. "High amplitude combustion instabilities in an annular combustor inducing pressure field deformation and flame blow off". *J. Eng. Gas Turb. Power,* **142**(1), p. 011016.

[33] Bourgouin, J.-F., Durox, D., Moeck, J. P., Schuller, T., and Candel, S., 2013. "Self-sustained instabilities in an annular combustor coupled by azimuthal and longitudinal acoustic modes". In Proc. ASME Turbo Expo, paper no. GT2013-95010.

[34] Rajendram Soundararajan, P., Durox, D., Renaud, A., and Candel, S., 2022. "Comparison of flame describing functions measured in single and multiple injector configurations". In Proc. ASME Turbo Expo 2022, paper no. GT2022-80577.

[35] Patat, C., Baillot, F., Blaisot, J.-B., and Domingues, E., 2021. "Responses of lean swirling spray flames to acoustic pressure and transverse velocity perturbations". In Symp. Thermoacoust. Combust.: Ind. meets Acad., paper no. 8499.

[36] Durox, D., Schuller, T., and Candel, S., 2005. "Combustion dynamics of inverted conical flames". *Proc. Combust. Inst.,* **30**(2), pp. 1717–1724.